UNIVERSITÄT AUGSBURG
Universitätsbibliothek

OPEN ACCESS
OPUS AUGSBURG

# Self-organization and collective migration of active condensates

**Hossein Vahid, Jens-Uwe Sommer, Abhinav Sharma**

**Angaben zur Veröffentlichung / Publication details:**

Vahid, Hossein, Jens-Uwe Sommer, and Abhinav Sharma. 2026. "Self-organization and collective migration of active condensates." *Communications Physics* 9 (1): 327. https://doi.org/10.1038/s42005-026-02903-1.

**Nutzungsbedingungen / Terms of use:**

**CC BY 4.0**

*Dieses Dokument wird unter folgenden Bedingungen zur Verfügung gestellt: / This document is made available under these conditions:*
***CC-BY 4.0: Creative Commons: Namensnennung***
*Weitere Informationen finden Sie unter: / For more information see:*
*https://creativecommons.org/licenses/by/4.0/deed.de*

communications physics

A Nature Portfolio journal

Article

https://doi.org/10.1038/s42005-026-02903-1

# Self-organization and collective migration of active condensates

Check for updates

Hossein Vahid [1], Jens-Uwe Sommer[1,2] ✉ & Abhinav Sharma [1,3] ✉

Cohesive active assemblies are often regulated by spatially heterogeneous nonequilibrium driving, such as gradients in motility. Here, we show that attractive active Brownian particles (ABPs) undergo liquid-gas phase separation, and spatially varying activity fields induce emergent dynamics. Attractive active droplets migrate up activity gradients, and at sufficiently high activity, they can fragment or evaporate into a dilute phase. For finite clusters, evaporated ABPs can redistribute through the simulation box, reassemble into new clusters in lower-activity regions, and migrate again toward higher activity regions. Even in the planar-slab geometry, migration toward higher activity and activity-controlled condensate stability persist, demonstrating the generality of these effects, while the geometry determines the pathway of particle redistribution and turnover. Within this model, these dynamics arise without biochemical feedback loops and rely only on the interplay of attraction, motility, and activity gradients. Our findings show how activity gradients can regulate the spatial localization, turnover, and repeated relocation of attractive active condensates.

Living systems organize matter in space by combining cohesive interactions with spatially heterogeneous sources of nonequilibrium driving[1–10]. At the subcellular scale, cells assemble biomolecular condensates that compartmentalize reactions without membranes[7,8,10–18], and at the tissue scale, they coordinate the directed migration of multicellular groups during development, wound repair, and disease[3,4,19–26]. In both settings, structure is not controlled by equilibrium thermodynamics alone; cellular assemblies are continually remodeled by energy-consuming processes and by gradients in the surrounding chemical or mechanical environment. Understanding how such gradients bias the position, stability, and turnover of cohesive assemblies is therefore a general problem in nonequilibrium soft matter.

Biomolecular condensates provide one important example of this principle. Many condensates are now understood as biomolecular assemblies with liquid-like properties, and their composition and material state are regulated by active biochemical processes[7,8,10,17]. ATP- and GTP-dependent enzymes, helicases, chaperones, phosphorylation cycles, and transport processes can all reshape condensate assembly and dissolution[7,11,12,14,16,17,27]. Moreover, ATP is not only an energy source but can also act directly as a hydrotrope that affects protein solubility at physiological concentrations[27]. These observations suggest that, in cells, spatial heterogeneity in metabolic or enzymatic activity can act as a spatially patterned nonequilibrium drive for condensate dynamics, even when there is no simple one-to-one correspondence between a condensate and a single control molecule.

At larger scales, collective cell migration is likewise controlled by spatial gradients[3,4,20–22,25,26]. Migrating cell groups respond to chemokines, growth factors, extracellular-matrix composition, stiffness, confinement, and intercellular communication[3,22,26,28,29]. These cues regulate local protrusion, traction, polarity, and persistence, allowing multicellular assemblies to move more efficiently and more persistently than isolated cells. From a coarse-grained physical perspective, such guidance can often be viewed as a spatial modulation of the local magnitude of active forcing, that is, of how strongly individual units are driven out of equilibrium.

The behavior of active particles in activity landscapes has been studied extensively for ideal and purely repulsive systems. Spatial variations in swim speed generate density contrasts, accumulation in low-motility regions, and interfacial polarization even in the absence of explicit alignment interactions; abrupt motility steps also produce characteristic pressure imbalances[30–32]. When the particles are cohesive, activity gradients no longer act on isolated particles only; they act on droplets or clusters whose interfacial polarization, internal turnover, and mechanical balance are all coupled to attraction.

Here, we study attractive active Brownian particles (ABPs) in a spatially varying activity field. Here, the activity field represents a spatial variation in the magnitude of self-propulsion. It may represent a coarse-grained description of spatially varying motility, traction, active stress, or the intensity of biochemical turnover that remodels an assembly. This formulation allows us to examine the physical consequence of combining

[1]Leibniz-Institut für Polymerforschung Dresden, Bereich Theorie der Polymere, Dresden, Germany. [2]Technische Universität Dresden, Institut für Theoretische Physik, Dresden, Germany. [3]Faculty of Mathematics, Natural Sciences, and Materials Engineering: Institute of Physics, University of Augsburg, Universitätsstraße 1, Augsburg, Germany. ✉e-mail: jens-uwe.sommer@tu-dresden.de; abhinav.sharma@uni-a.de

cohesion with heterogeneous driving, without relying on the microscopic details of any one biological system. In the parameter ranges studied, this setting produces several forms of self-organization, including localized steady-state turnover in the planar-slab geometry and repeated relocation events in the finite-cluster geometry over the simulated time window. These two geometries provide complementary tests of the same underlying physics. Activity gradients generate asymmetric interfacial forcing that drives attractive condensates toward higher activity, while the competition between activity and cohesion controls their stability and turnover. The finite-cluster geometry removes the transport constraint imposed by an extended slab, demonstrating that these central physical conclusions do not depend on the planar-slab geometry itself. This behavior arises without any biochemical feedback or external control but as an emergent consequence of the interplay between attraction and activity gradients. Our results, therefore, identify a minimal physical route by which cohesive active matter can self-organize, relocate, and renew under heterogeneous nonequilibrium driving.

## Methods

We perform Brownian dynamics (BD) simulations of ABPs in a rectangular box of dimensions $L_x \times L_y \times L_z$. Each ABP experiences the self-propulsion force $\boldsymbol{F}_{\mathrm{a}}^i = f_{\mathrm{a}}\boldsymbol{e}^i$, where $f_{\mathrm{a}}$ represents the magnitude of the active force, and $\boldsymbol{e}^i$ is a unit vector denoting the instantaneous propulsion direction of the particle. The equation of motion of the $i$-th ABP is expressed by $\gamma_{\mathrm{t}}\dot{\boldsymbol{r}}^i = -\sum_j \nabla_{\boldsymbol{r}^i} U^{ij} + \boldsymbol{F}_{\mathrm{a}}^i + \boldsymbol{\xi}(t)$, where $\gamma_{\mathrm{t}}$ is the translational friction coefficient, $U^{ij}$ the inter-particle interaction potential, and $\boldsymbol{\xi}^i(t)$ a Gaussian white noise term satisfying $\langle \boldsymbol{\xi}^i(t)\rangle = 0$ and $\langle \xi_\alpha^i(t)\xi_\beta^j(t')\rangle = 2\gamma_{\mathrm{t}}^{-1}k_{\mathrm{B}}T\delta^{ij}\delta_{\alpha\beta}\delta(t-t')$. Here, $\alpha, \beta \in \{x, y, z\}$, and $k_{\mathrm{B}}T = \beta^{-1}$ is the thermal energy, with $k_{\mathrm{B}}$ the Boltzmann constant and $T$ the temperature. The orientation $\boldsymbol{e}^i$ evolves via rotational diffusion given by $\dot{\boldsymbol{e}}^i = \boldsymbol{e}^i \times \boldsymbol{\eta}(t)$, where $\boldsymbol{\eta}(t)$ is a Gaussian white noise angular velocity vector having zero mean and correlations $\langle \eta_\alpha^i(t)\eta_\beta^j(t')\rangle = 2\gamma_{\mathrm{r}}^{-1}k_{\mathrm{B}}T\delta^{ij}\delta_{\alpha\beta}\delta(t-t')$, with $\gamma_{\mathrm{r}}$ denoting the rotational friction coefficient.

Pairwise interactions of two ABPs at distance $r$ are modeled via the Wang-Frenkel potential[33]: $U_{\mathrm{WF}}(r) = \epsilon\left[(\sigma/r)^2 - 1\right]\left[(r_{\mathrm{c}}/r)^2 - 1\right]^2\Theta(r_{\mathrm{c}}-r)$, where $r$ is their distance, $\epsilon$ the potential well depth, $\sigma$ the diameter of ABPs, $\Theta$ is the Heaviside step function, and $r_{\mathrm{c}} = 2\sigma$ the cut-off distance. The latter results in a Lennard-Jones-like behavior[33], and the potential quadratically vanishes at $r_{\mathrm{c}}$, ensuring the pair force disappears continuously. We use reduced units by setting $\sigma = 1$, $k_{\mathrm{B}}T = 1$, and $\tau = \gamma_{\mathrm{r}}/k_{\mathrm{B}}T = 1$, which define units of length, energy, and time, respectively. The equations of motion are integrated using a timestep $5 \times 10^{-4}\tau$. We set $\gamma_{\mathrm{r}} = \gamma_{\mathrm{t}}\sigma^2/3$, the Péclet number in homogeneous activity is defined as $\mathrm{Pe} = f_{\mathrm{a}}\sigma/k_{\mathrm{B}}T$, and $\rho_0$ is the bulk density of ABPs. Simulations and visualizations are performed using LAMMPS[34] and OVITO[35] packages, respectively.

## Results and Discussion

### Phase behavior and interfacial mechanics of attractive ABPs

To characterize the self-assembly and collective organization of attractive ABPs, we study their phase behavior by systematically varying $\epsilon$ across different Pe using direct coexistence simulations[36–39] (computational details are provided in the Supplementary Information). The phase diagrams in Fig. 1b reveal vapor-liquid coexistence, showing how cohesive interactions drive cluster formation. For a fixed Pe and a given attraction strength $\epsilon$, the dilute and condensed coexistence densities ($\rho$) are obtained from the two branches of the binodal. As $\epsilon$ increases at fixed Pe, the horizontal separation between the dilute and dense branches of the binodal becomes larger, indicating an increasing density contrast between the coexisting phases. Increasing Pe broadens the coexistence region in both density and attraction strength, shifting the binodal to higher $\rho$ and higher $\epsilon$; in other words, stronger cohesion is needed to maintain phase separation at higher activity, and the critical density and attraction ($\rho^*, \epsilon^*$) increase accordingly (see Table SI). These trends are consistent with experiments: motile *E. coli* require stronger attractions to phase-separate than passive suspensions[40,41], and higher ATP levels fluidize nucleoli, whereas ATP depletion stiffens them[11,12].

Beyond bulk densities, the structural organization at the vapor-liquid interfaces provides insight into self-assembly dynamics. We quantify particle alignment across the vapor-liquid interface through the orientation parameter $\langle e_z(z)\rangle = \frac{1}{N_z}\left\langle \sum_{i\in z} \boldsymbol{e}^i \cdot \hat{\boldsymbol{z}}\right\rangle_t$, where $N_z$ is the number of particles at position $z$, $\hat{\boldsymbol{z}}$ the unit vector along the $z$-axis, and $\langle\cdot\rangle_t$ indicates the time average. Figure 1c shows that ABPs display outward polarization from the dense liquid phase at the interfaces. At fixed $\epsilon/\epsilon^* = 1.7$, the alignment intensifies as Pe increases. Alignment is negligible within bulk phases and along tangential directions $\langle e_x(z)\rangle = \langle e_y(z)\rangle = 0$ [36–38]. Instantaneous in-plane velocity streamlines, calculated from the $x$- and $y$-components of the particle velocities within $xy$-slices of thickness $2\sigma$, are shown in Fig. 1d–f. The slices are centered at $z = -7$, $z = 0$, and $z = 7$. Near the interfaces at $z = \pm 7$, the in-plane motion is enhanced and contains locally circulating streamline patterns, whereas the central region at $z = 0$ shows slower and more disordered motion.

To quantify mechanical stresses across the inhomogeneous system, we calculate the spatial profile of the normal pressure along the $z$-direction. The local normal pressure is decomposed into ideal, interaction, and active contributions as

$$P_{\mathrm{tot}}(z) = P_{\mathrm{id}}(z) + P_{\mathrm{vir}}(z) + P_{\mathrm{act}}(z). \tag{1}$$

The ideal contribution is obtained from the local number density profile as

$$P_{\mathrm{id}}(z) = \rho(z)k_{\mathrm{B}}T. \tag{2}$$

The interaction contribution $P_{\mathrm{vir}}(z)$ is obtained from the slab-resolved configurational stress profile normal to the $z$-direction, using the same pressure sign convention as in the total normal pressure. For a slab of volume $V_k = A\Delta z$, where $A$ is the cross-sectional area and $\Delta z$ is the bin width, the configurational contribution can be expressed in an Irving–Kirkwood form as[42]

$$P_{\mathrm{vir}}(z_k) = \left\langle \frac{1}{2V_k}\sum_i \sum_{j\neq i}\left[-F_z^{ij}(z_b - z_a)\right]\right\rangle. \tag{3}$$

Here, $F_z^{ij}$ is the $z$-component of the force exerted by particle $j$ on particle $i$, and $z_a$ and $z_b$ denote the entry and exit positions of the Irving–Kirkwood contour through slab $k$. Thus, each interacting pair contributes in proportion to the fraction of its contour contained within the slab.

The active contribution is calculated from the slab-resolved polarization density[43]

$$m_z(z_k) = \left\langle \rho(z_k, t)\langle e_z\rangle_k(t)\right\rangle_t. \tag{4}$$

Here, $\langle e_z\rangle_k(t)$ denotes the average orientation of particles located in the slab $k$ centered at $z_k$ at time $t$, and $\langle\cdots\rangle_t$ denotes an average over the selected steady-state time window. For propulsion strength $f_{\mathrm{a}}(z)$, this results in the local active body-force density

$$b_{\mathrm{act}}(z) = f_{\mathrm{a}}(z)\, m_z(z) = f_{\mathrm{a}}(z)\left\langle \rho(z,t)\langle e_z\rangle(z,t)\right\rangle_t. \tag{5}$$

The active contribution to the normal pressure is then obtained by integrating this body-force density along $z$, $P_{\mathrm{act}}(z) = -\int_{z_{\mathrm{ref}}}^{z} b_{\mathrm{act}}(z')\,dz'$. Here, $z_{\mathrm{ref}}$ denotes the reference position used to set the additive constant of the integrated active contribution. The integration is performed over the entire simulation domain, $z_{\min} \le z \le z_{\max}$, with $z_{\mathrm{ref}} = z_{\min}$. The lower boundary $z_{\min}$ is located in the dilute region, where $b_{\mathrm{act}}(z_{\min}) \simeq 0$. In

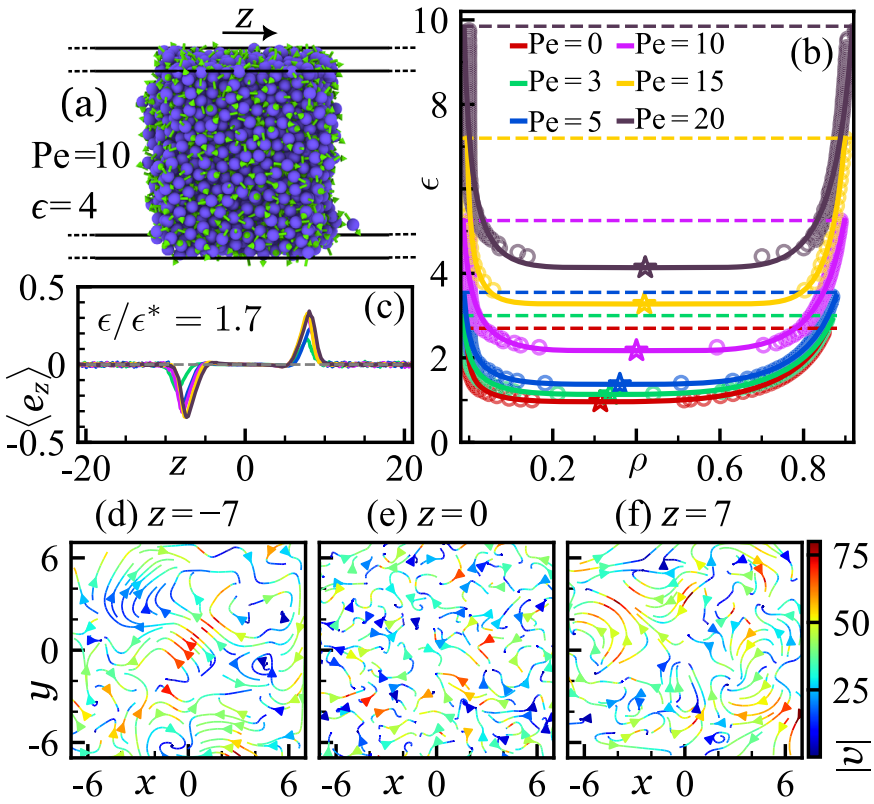



**Fig. 1 | Phase behavior and interfacial dynamics of attractive ABPs. a** A snapshot of the simulation box for Pe = 10 and $\epsilon = 4$. The system exhibits phase coexistence, with a dense liquid-like slab at the center surrounded by a dilute vapor phase. **b** Phase diagrams as a function of attraction strength $\epsilon$. Circles indicate simulation points, solid lines are fits to Eq. (S1), and dashed lines are the approximate $\epsilon$ values beyond which the system transitions to a densely-packed phase. Star symbols indicate the estimated critical points ($\rho^*$, $\epsilon^*$). **c** Profile of the average propulsion direction along $z$-axis, $\langle e_z(z)\rangle$, for various Pe at fixed $\epsilon/\epsilon^* = 1.7$. Legends of (**b**) also apply to (**c**). **d**–**f** Velocity streamlines at the interfaces of the condensed phase $z = \pm 7$ and at the center of condensate $z = 0$. Here, Pe = 10 and $\epsilon = 4$.

practice, this integral is evaluated numerically using the trapezoidal rule on the same $z$-grid as the density and stress profiles.

We also compute the corresponding $z$-resolved force contribution in each slab. Thus, for the ideal and virial contributions,

$$F_{\mathrm{id}}(z) = -A\Delta z\frac{dP_{\mathrm{id}}}{dz} = -A\Delta z\, k_{\mathrm{B}}T\frac{d\rho}{dz}, \qquad F_{\mathrm{vir}}(z) = -A\Delta z\frac{dP_{\mathrm{vir}}}{dz}. \quad (6)$$

For the active contribution, the slab-resolved force is obtained directly from the active body-force density,

$$F_{\mathrm{act}}(z) = A\Delta z\, b_{\mathrm{act}}(z). \quad (7)$$

Here $\Delta z = 0.1$ is the bin width used in the profile calculation. The total slab-resolved force is then

$$F_{\mathrm{tot}}(z) = F_{\mathrm{id}}(z) + F_{\mathrm{vir}}(z) + F_{\mathrm{act}}(z). \quad (8)$$

Figure 2 shows the decomposition of the normal pressure and the corresponding slab-resolved force contributions for a representative system with 5000 ABPs in a $15 \times 15 \times 80$ simulation box at Pe = 20 and $\epsilon = 6$. Panel (a) shows the ideal, virial, and active pressure profiles. The ideal pressure increases within the dense phase, indicating a higher local density. The virial pressure is negative and develops pronounced minima at the interfaces, because attractive interactions generate a tensile configurational stress where the density changes rapidly. In contrast, the active pressure shows positive interfacial peaks. These peaks result from the interfacial polarization of ABPs, which produces a localized active body-force density $b_{\mathrm{act}}(z) = f_{\mathrm{a}}(z)\, m_z(z)$. The active pressure, obtained by integrating this body-force density, therefore varies most strongly across the interfacial regions. Although the individual ideal, virial, and active pressure contributions are large, their sum remains nearly flat, indicating that the system is close to mechanical balance in the steady state.

The corresponding bin-resolved forces in Fig. 2b are localized at the interfaces because they are proportional to the gradients of the pressure profiles. The large positive and negative peaks in $F_{\mathrm{id}}$, $F_{\mathrm{vir}}$, and $F_{\mathrm{act}}$, therefore, reflect the sharp interfacial variations of the corresponding pressure terms. Their strong cancellation gives a nearly vanishing total force $F_{\mathrm{tot}}$, consistent with the nearly constant total pressure in Fig. 2a.

### Migration and localization in activity gradients

We now turn to how an attractive ABP condensate responds to activity gradients. To this end, we conduct BD simulations of a condensate of 5000 ABPs placed at $-40 \le z \le -10$ within a periodic box of size $15 \times 15 \times 80$, with activity varying only along the $z$-axis, $f_{\mathrm{a}}(z) = 20\left(1 - |z|/40\right)$, peaking at $z = 0$ and vanishing at $z = \pm 40$ (Fig. 3(a)). Figure 3(b) shows steady-state density profiles along $z$ for various $\epsilon$. At weak attraction ($\epsilon = 1$), activity overwhelms cohesion; the droplet evaporates, and ABPs disperse, accumulating in low-activity regions. At strong cohesion ($\epsilon > 5$), the parent droplet remains intact and migrates as a single self-propelled entity to $z = 0$ (highest-activity region).

At moderate attraction strengths ($\epsilon = 2 - 4$), droplets climb the gradient but are fragile; the parent droplet fissions into two daughter droplets that settle in intermediate-activity regions where active and attractive forces roughly balance. This macroscopic behavior is accompanied by continuous microscopic turnover: ABPs detach from and rejoin the condensates while the droplets remain statistically localized. Such continuous assembly and disassembly is characteristic of *living clusters*. Active systems often form living clusters that continually assemble and break apart under the balance of self-propulsion and cohesion[44–48], as seen in active colloids and light-activated Janus living crystals[47]. Analogous turnover and reorganization processes occur in cell collectives when adhesion competes with motility[49]. As shown in Figs. 3(c), ABPs at the condensate interfaces exhibit an outward orientation from the dense phase. Figure S3 shows that, at fixed volume, increasing ($N$) from 2500 to 5000 produces broader, more massive condensates while preserving their localization behavior.

Figure 3e–l quantify this behavior by tracking the droplet size $N(t)$ and its center-of-geometry $z_{\mathrm{COG}}(t)$ along the activity gradient over the final $10^5\tau$ of simulation trajectories. At intermediate attraction strengths $\epsilon = 2$–4, the daughter droplets exhibit steady-state turnover. Their sizes fluctuate around

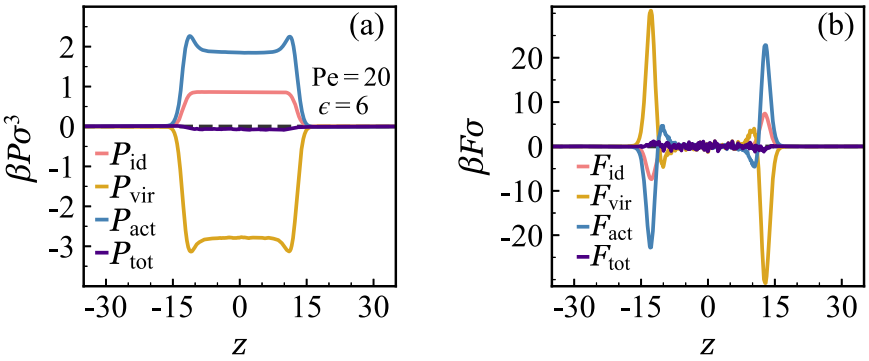



**Fig. 2 | Pressure and force-balance decomposition for a representative system at Pe = 20 and $\epsilon = 6$.** **a** Normal pressure profiles $P_{id}$, $P_{vir}$, $P_{act}$, and $P_{tot}$. The total pressure remains nearly flat because the ideal, virial, and active contributions compensate each other. **b** Corresponding slab-resolved force contributions $F_{id}$, $F_{vir}$, $F_{act}$, and $F_{tot}$, obtained using $A\Delta z$ times the local force densities. The individual force contributions are localized at the interfaces and cancel, giving a zero net total force.

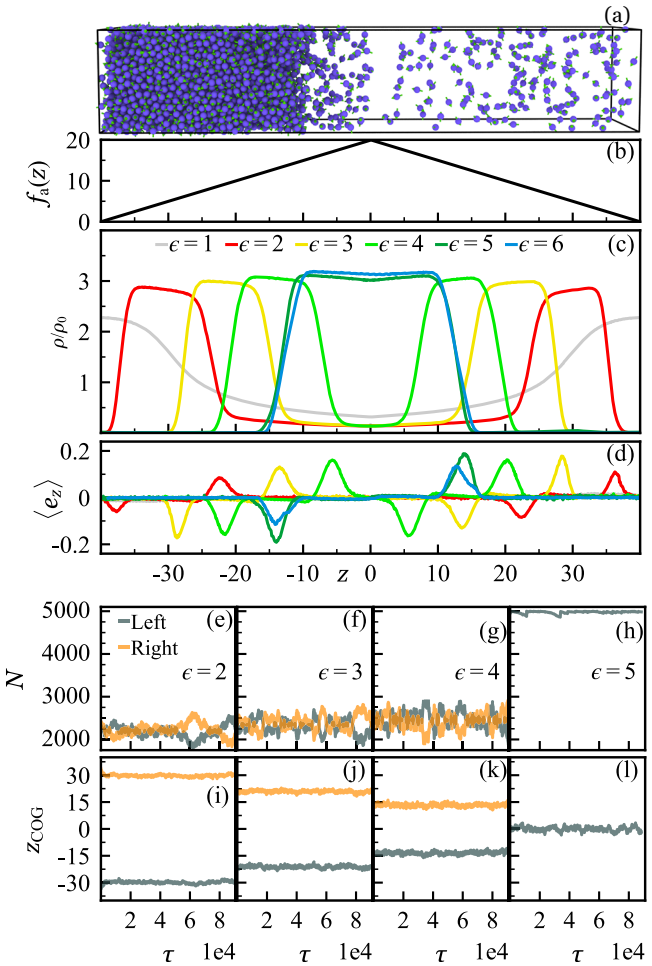



**Fig. 3 | Migration, splitting, and localization of active condensates in an activity gradient.** **a** Initial configuration at time $t = 0$, showing a dense droplet with $\epsilon = 4$ and $N = 5000$ placed on the left side of the box ($z < -10$), where activity is lowest. **b** Activity profile $f_a$ as a function of $z$. The activity field is given by $f_a(z) = 20(1 - |z|/40)$, creating a linear gradient symmetric about $z = 0$. **c** Steady-state normalized density profiles $\rho(z)/\rho_0$ for varying $\epsilon$. Additional results for other $N$ and activity gradient steepness are presented in Fig. S3. **d** Steady-state profiles of the ABP propulsion direction projected along the $z$-axis, $\langle e_z(z) \rangle$. **e–h** Time evolution of the droplet size $N(t)$, defined as the number of ABPs in each daughter droplet, for $\epsilon = 2$, 3, 4, and 5, respectively. The two curves correspond to the left and right droplets. **i–l** Corresponding time evolution of the droplet center-of-geometry along the activity-gradient direction, $z_{COG}(t)$, for the same values of $\epsilon$. For $\epsilon = 5$, only a single trace is present because the droplet does not split.

a mean value, indicating continuous exchange of ABPs with the surrounding dilute phase, and their centers of geometry remain statistically stable. Increasing the attraction strength to $\epsilon \geq 5$ stabilizes the condensates against activity-induced deformation and particle loss. The corresponding time traces reveal larger condensed masses as well as smaller fluctuations in both $N(t)$ and $z_{COG}(t)$.

Figure 4 shows the pressure decomposition for attractive ABP condensates at $\epsilon = 4$ in the spatial activity gradient $f_a(z) = 20(1 - |z|/40)$. Panel (a) shows the steady-state configuration, where the condensates are not constrained. Panels (b) and (c) show constrained configurations in which the condensates are held away from this steady-state position by re-centering them at each time step. In panel (b), the condensates are kept farther from the activity maximum, $z_{COG}^{L,R} = \mp 22$, whereas in panel (c), they are kept closer to the activity maximum, $z_{COG}^{L,R} = \mp 12$. The individual pressure contributions are asymmetric across each daughter droplet because the inner and outer interfaces experience different local activities and interfacial structures. Here, the inner and outer interfaces denote the side of each condensate facing the high- and low-activity regions, respectively. The ideal pressure follows the density profile and is larger where the local density is higher. Since the higher activity near the inner interfaces enhances particle exchange and particle loss from the condensate, the density, and therefore $P_{id}$, can decrease from the outer to the inner side. The virial pressure is negative and develops pronounced interfacial minima due to attractive configurational stresses. The active pressure shows interfacial peaks arising from the polarization-induced active body-force density.

In the steady state [Fig. 4a], these asymmetric contributions compensate so that $P_{tot} = P_{id} + P_{vir} + P_{act}$ is nearly flat, indicating mechanical balance. When the condensates are displaced from this position, the compensation is incomplete and results in nonuniform $P_{tot}$. For condensates held farther from the activity maximum [Fig. 4b], the total-pressure imbalance corresponds to an inward mechanical drive, which would move the condensates toward the high-activity region if they were not re-centered. In contrast, when the condensates are held closer to the activity maximum than their steady-state position [Fig. 4c], the imbalance changes sign, indicating a restoring tendency away from the center.

To quantify the mechanical imbalance, we determine the two interface positions of each condensate from the time-averaged density profile. The net inward force on a condensate is calculated from the total-pressure difference between its outer and inner interfaces, $F_{net} = A\left[P_{tot}^{out} - P_{tot}^{in}\right]$, where $P_{tot}^{out}$ and $P_{tot}^{in}$ are the total pressures at the outer and inner interfaces, respectively. With this convention, $F_{net} > 0$ corresponds to a force toward the activity maximum, whereas $F_{net} < 0$ corresponds to a force away from it. To this end, we calculate the net force from constrained simulations in which the two condensates are held at prescribed positions, $z_{COG}^{L,R} = \mp d$, by re-centering them at each time step. The net force is obtained for each imposed distance $d = |z_{COG}|$, and we report the average net force by averaging over the left and

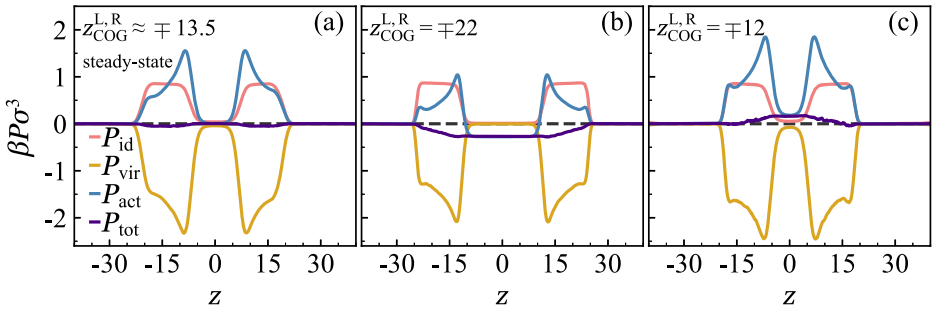



**Fig. 4 | Pressure decomposition in the activity gradient $f_a(z) = 20(1 - |z|/40)$ at $\epsilon = 4$.** **a** Steady-state pressure profiles for unconstrained condensates. **b** Pressure profiles for condensates constrained farther from the activity maximum, $z_{COG}^{L,R} = \mp 22$. **c** Pressure profiles for condensates constrained closer to the activity maximum than their steady-state position, $z_{COG}^{L,R} = \mp 12$. The curves show the ideal, virial, active, and total normal pressure contributions, $P_{id}$, $P_{vir}$, $P_{act}$, and $P_{tot}$, respectively.

right condensates. The position-dependent drift velocity can also be calculated independently from unconstrained simulations. For each value of $\epsilon$, we perform 400 simulations with independent random seeds and follow the motion for $2 \times 10^4 \tau$. At each recorded frame, the centers of geometry of each daughter droplet, $z_{COG}^{L}(t)$ and $z_{COG}^{R}(t)$, are calculated. The inward drift velocity is obtained from finite-time displacements,

$$v_{in}(d) = -\left\langle \frac{d(t+\tau) - d(t)}{\tau} \right\rangle_{d(t)\in[d-\Delta d/2, d+\Delta d/2]}, \tag{9}$$

where the average is taken over both condensates and all independent simulations. Since the condensates can exchange particles with the dilute phase and their sizes vary with time, the velocity average is weighted by the instantaneous condensate size, $\langle v_{in}(d)\rangle = \frac{\sum_s N_s v_s(d)}{\sum_s N_s}$, where $N_s$ is the number of particles in the condensate associated with sample $s$. With this convention, positive $v_{in}$ denotes migration toward $z = 0$.

Figure 5 shows that the mechanically calculated forces and the independently calculated drift velocities are consistent. In the range where the condensates migrate toward the activity maximum, $F_{net}$ is positive, and $v_{in}$ is also positive. Both quantities exhibit a maximum at intermediate distances and decrease as the condensates approach their steady-state positions. The two curves are not expected to collapse point by point because the drift velocity also depends on an effective mobility, which varies with condensate size, shape, and particle exchange with the dilute phase. The time-dependent trajectories in Fig. 5c provide the corresponding time view of this migration process. Starting from condensates located away from the activity maximum, the mean distance $d(t)$ decreases with time, demonstrating net inward motion toward the high-activity region. At later times, $d(t)$ approaches a plateau, indicating that the condensates reach statistically steady positions. The plateau position depends on $\epsilon$, consistent with the force and velocity profiles in Fig. 5a, b: condensates migrate inward over the range where $F_{net} > 0$ and $v_{in} > 0$, and slow down as they approach their steady-state locations. Figure 5d shows the corresponding evolution of the mean condensate size, $\langle N_s\rangle$. As the condensates migrate toward the activity maximum, $\langle N_s\rangle$ decreases, indicating partial loss of condensed particles due to stronger activity in the central region. At later times, when the condensates approach their steady-state positions, $\langle N_s\rangle$ also reaches an approximately constant value. For the weakest attraction shown, $\epsilon = 2$, the fluctuations around the mean are larger than for higher $\epsilon$, indicating weaker cohesion and stronger exchange of ABPs between the condensates and the surrounding dilute phase.

### Finite-cluster dynamics and geometry dependence

To further investigate this phenomenon for finite clusters, we conduct simulations of 5000 attractive ABPs under a spatially varying activity field. The ABPs are randomly initialized in a cubic box of size $50^3$, with harmonic, repulsive walls that keep them within $z \in [-25, 25]$ (cf. Suppl. Note 1). Periodic boundary conditions are imposed along the $x$ and $y$ directions. The propulsion force of each ABP increases linearly along the $z$-axis, defined by $f_a(z) = 20(z + 25)/50$. Figure 6a shows the resulting steady-state density profiles for different attraction strengths $\epsilon$. At $\epsilon = 1$, the attraction is weak to support stable aggregates, and ABPs mainly accumulate in the low-activity region. At intermediate attraction strengths $\epsilon = 2 - 6$, finite clusters nucleate preferentially in the low-activity region and migrate toward higher activity (see Movie S1). The position of the density peak shifts progressively toward higher $z$ as $\epsilon$ increases, showing that stronger cohesion allows clusters to penetrate farther into the high-activity region. For sufficiently strong attraction, as in the $\epsilon = 7$ case, the system forms a densely packed aggregate that remains localized in the highest-activity region with suppressed particle loss.

The migration toward higher activity is associated with interfacial orientational polarization. As shown in Fig. 6b, ABPs at the droplet interfaces orient outward from the dense phase (Fig. 6b); see also refs. 36–38. ABPs on the high-activity side experience stronger propulsion, and the outward orientation ordering of interfacial ABPs generates a net force toward regions of higher activity. Qualitatively, it is analogous to active colloidal dimers with opposite orientations, which tend to accumulate in high-activity regions[50]. At $\epsilon = 7$, the condensates are densely packed, and the interfacial polarization decreases significantly compared to liquid-like condensates $\epsilon < 7$ (see Fig. 6b). However, this weak polarization is still sufficient to drive the condensate to high-activity regions. We quantify the aggregation–fragmentation dynamics over a short time interval of $10\tau$ using transition matrices, $\Pr(N_1|N_0, \Delta t = 10\tau)$, shown in Fig. 6c–g. These matrices give the conditional probability that a cluster of size $N_0$ evolves into a cluster of size $N_1$ after a time interval $\Delta t = 10\tau$. The probability is concentrated near the diagonal $N_1 \simeq N_0$, indicating that most clusters change size gradually over this time scale rather than undergoing abrupt dissolution and reformation. The off-diagonal weight near the diagonal corresponds to the gain or loss of particles by exchange with the surrounding dilute phase. For weaker attractions, the probability distribution is broader, indicating stronger cluster-size fluctuations and more frequent particle exchange. As $\epsilon$ increases, the probability becomes more concentrated near the diagonal $N_1 \simeq N_0$, and probability weight appears at larger values of both $N_0$ and $N_1$, showing that stronger cohesion supports larger clusters.

The finite-cluster geometry provides a test of whether the behavior identified above is specific to the planar-slab configuration. In both geometries, common physical responses to the activity gradient are observed. Attractive condensates exhibit outward interfacial polarization and migrate toward higher activity, while increasing activity promotes particle loss and competes with cohesion. The geometries differ, however, in how evaporated particles can redistribute. In the planar-slab geometry, the dense phase spans the simulation box in the two directions perpendicular to the activity gradient, so that the two condensates form extended slabs on opposite sides of the activity maximum. ABPs evaporating from the interfaces facing the high-activity region remain confined between these slabs and cannot bypass them to reach the low-activity sides. In the finite-cluster geometry, by contrast, evaporated ABPs can move around the clusters and redistribute freely through the dilute phase. They can subsequently nucleate new clusters in lower-activity regions, which again migrate toward higher activity. Thus, the slab geometry affects the global redistribution pathway and leads to a localized steady-turnover state, whereas finite clusters permit repeated

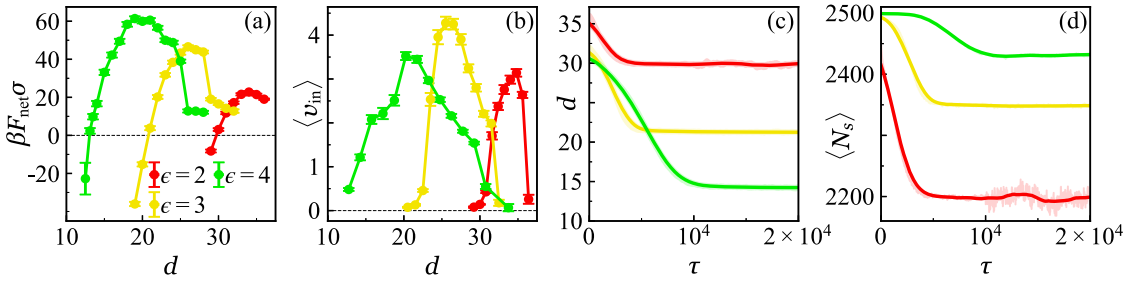



**Fig. 5 | Mechanical force and drift dynamics of attractive active condensates in the activity gradient $f_a(z) = 20(1 - |z|/40)$.** **a** Net inward force $F_{net}$ as a function of the imposed condensate distance from the activity maximum, $d = |z_{COG}|$, for different attraction strengths $\epsilon$. Positive values correspond to a force toward the activity maximum at $z = 0$. For each combination of $d$ and $\epsilon$, $n = 1$ constrained simulation is performed. The reported force is averaged over the left and right condensates, and the error bars represent the propagated jackknife standard error calculated from 5000 time-resolved profiles. **b** Position-dependent inward drift velocity $\langle v_{in}(d)\rangle$, plotted in units of $10^{-3}\sigma/\tau$, calculated from unconstrained migration simulations. The velocity average is weighted by the instantaneous condensate size $N_s$. **c** Time evolution of the mean condensate distance $d$ from the activity maximum, showing migration toward the activity maximum and the approach to a steady-state position. **d** Corresponding time evolution of the mean condensate size, $\langle N_s\rangle$, showing that the condensates remain finite while migrating and approaching their steady-state positions. For panels (**b**–**d**), $n = 400$ independent simulations with different random seeds are performed for each $\epsilon$, with each simulation run for $2 \times 10^4\tau$. Pale-shaded regions in panels (**c**, **d**) indicate the standard error of the mean across these independent simulations.

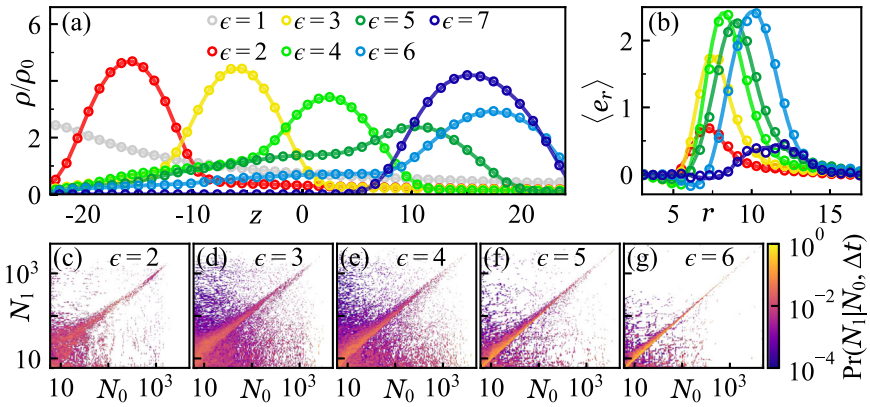



**Fig. 6 | Localization, radial polarization, and size dynamics of finite active clusters.** **a** Steady-state density profile of ABPs along the z axis. The activity field is given by $f_a(z) = f_a^*(z + 25)/50$, with $f_a^* = 20$. The system along the z-axis is non-periodic. **b** $\langle e_r\rangle = \langle \Sigma_{i\in r} \boldsymbol{e}^i \cdot \hat{\boldsymbol{r}}\rangle_t$ for the largest cluster as a function of $r$ from the cluster center-of-geometry, averaged over time. **c**–**g** Transition matrix $P(N_1|N_0, \Delta t)$ for varying $\epsilon$, with $\Delta t = 10\tau$. Results for $f_a^* \in \{10, 40, 80\}$ are presented in Figs. S5 and S6.

nucleation, migration, and evaporation. Importantly, the common migration toward higher activity and the coupling between activity, interfacial polarization, and condensate stability persist in both geometries, showing that these central conclusions are not consequences of the geometric constraint imposed by the planar slabs.

Figure 7 shows the time evolution of the cluster size $N_c(t)$ and the corresponding center-of-geometry position $z_{COG}(t)$ during the final $10^5\tau$. Different colors denote different tracked clusters, so that the size and position of the same cluster can be compared between the upper and lower panels. For weak attraction, $\epsilon = 2$, the clusters remain relatively small and fluctuate near the lower-activity region. For intermediate attractions, $\epsilon = 3$–$6$, clusters typically appear in the lower-activity region, grow there, and then migrate toward larger $z$, corresponding to regions of higher activity. The largest value of $z_{COG}$ reached by a cluster increases with $\epsilon$, showing that stronger cohesion allows clusters to penetrate farther into the high-activity region before losing stability. Comparing $N_c(t)$ with $z_{COG}(t)$ for each tracked cluster shows that cluster nucleation occurs mainly in the lower-activity region, whereas shrinkage and evaporation occur after the cluster has migrated into higher-activity regions. New clusters appear at later times in the lower-activity regions from ABPs that had previously evaporated and redistributed through the dilute phase. Cluster trajectories that end within the plotted time window without $N_c$ approaching zero indicate merging with another cluster. The dynamics, therefore, involve continuous cluster birth in low-activity regions, growth and migration toward higher activity, and subsequent evaporation or merging. For the strongest attraction shown, $\epsilon = 7$, ABPs remain in an almost fully condensed aggregate with little particle loss, indicating that strong cohesion suppresses the evaporation observed at intermediate attraction strengths.

### Role of interfacial polarization in migration direction

What role does interfacial polarization play in this behavior? To address this question, we compare an active condensate in an activity gradient to a passive condensate in a thermal gradient (computational details are provided in Supplementary Note 2). In active systems, high-activity regions are analogous to hot regions in passive systems[51–53]. Models based on interfacial pressure predict that both droplets should migrate toward the colder or low-activity region[51–55]. Our simulations recapitulate this expected behavior for the passive droplet (see Fig. 8a). In contrast, the active condensate migrates toward the high-activity region (Fig. 8b). For the cases examined here, the opposite migration direction shows that the behavior cannot be captured by a passive thermophoretic droplet picture or by a scalar effective-temperature mapping. A relevant difference is that attractive active condensates develop a distinct interfacial orientational polarization, which produces an active body-force density $b_{act}(z) = f_a(z)\rho(z)\langle e_z(z)\rangle$. The resulting active pressure imbalance can drive motion toward higher activity, opposite to the passive case (see Fig. S7 for pressure profiles). We also perform simulations for ABP clusters formed by motility-induced phase separation (MIPS) using hard-sphere ABPs (without pair-attractions). For these clusters, the propulsion direction at the liquid-gas interface points toward the condensed phase[43,56], and consequently, the clusters migrate toward regions of low activity (Fig. 8c). These results reveal that the orientational ordering of ABPs plays an important role in determining the migration direction. In panel (c), the

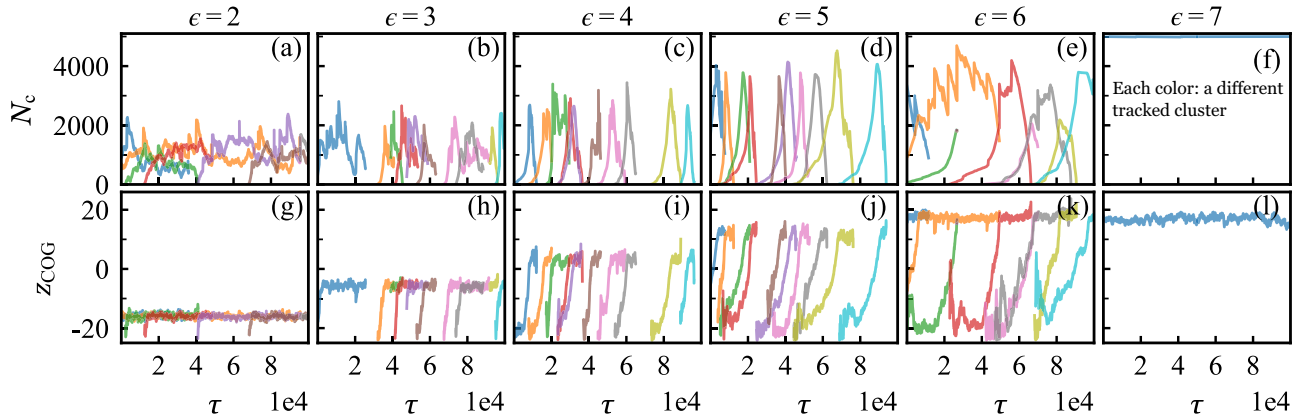



**Fig. 7 | Cluster tracking in the activity gradient for the systems shown in Fig. 6, calculated during the final $10^5\tau$. a–f** Time evolution of the cluster size $N_c(t)$ for tracked clusters at $\epsilon$ = 2, 3, 4, 5, 6, and 7, respectively. **g–l** Corresponding center-of-geometry position $z_{COG}(t)$ along the activity-gradient direction. Different colors correspond to different tracked clusters. For intermediate attractions, $\epsilon$ = 3–6, individual clusters can grow to large sizes, migrate to higher $z$, and then shrink and disappear while new tracked clusters appear at later times. Cluster trajectories that terminate within the plotted time window before $N_c$ decreases to zero indicate that the corresponding cluster has merged with another. At the strongest attraction shown, $\epsilon$ = 7, the system forms an almost fully condensed aggregate with little particle loss over the observation time. Animations of the simulations are provided in Movie S1.

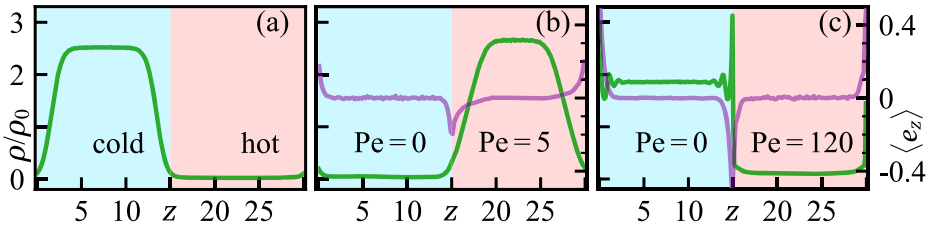



**Fig. 8 | Contrasting responses of passive, attractive active, and MIPS condensates to spatial gradients.** Steady-state density profiles ($\rho/\rho_0$, green, left axis) and $\langle e_z \rangle$, purple, right axis) for: (**a**) a passive condensate in a thermal gradient; (**b**) an attractive active condensate in an activity gradient; (**c**) a MIPS cluster in an activity gradient. Simulation animations are presented in Movie S2. In the passive reference simulation, the temperature gradient is generated by adding kinetic energy to the hot slab and removing the same amount from the cold slab, producing a stationary temperature profile along $z$ (see Supplementary Note 2).

interface exhibits strong oscillations in the density profile. Particles that move from the region with Pe = 120 into regions with Pe = 0 lose their self-propulsion and pile up near the interface, creating an over-compressed first layer. Steric packing behind this layer then produces a sequence of oscillations in the density profile. The density profile near the interface is reminiscent of packing-induced layering in dense passive colloidal systems confined by soft repulsive walls; see Fig. S8 and refs. 57,58.

## Conclusions

Cohesive active assemblies can display emergent, group-level responses to spatial cues. For example, in biological active matter, groups of cells can respond collectively to spatial guidance cues that are weak or absent at the single-cell level[22,28,29,59,60]. Our results show that group-level responses to spatial gradients can arise in a minimal active-matter setting, where cohesion and spatially varying activity generate condensate migration, localization, and turnover. Interparticle attraction drives liquid-gas transition, and the competition between self-propulsion and attraction determines their directional transport. We find that the direction of motion is determined by the preferential orientation of ABPs at the droplet interface, while the interior remains disordered. In the strong-attraction regime, stable, giant clusters form and are driven to regions of highest activity. At intermediate attraction strengths, a dynamic living state emerges, characterized by clusters that fragment and reassemble. These living clusters reside in intermediate activity regions. Adding passive, less cohesive particles stabilizes the living clusters, which migrate toward higher-activity regions. The comparison between planar slabs and finite clusters further shows that the central response is not specific to the slab geometry. In both cases, interfacial polarization in an activity gradient drives attractive condensates toward higher activity, and the competition between activity and cohesion governs their stability and particle exchange. Geometry primarily determines how particles released from a condensate can redistribute. Extended slabs restrict this transport and favor localized steady-state turnover, whereas finite clusters allow particles to bypass the condensate, redistribute through the dilute phase, and generate repeated nucleation-migration-evaporation events.

Our findings contrast with MIPS clusters, where inward-pointing particles at the interface drive condensates toward low activity. This highlights that a theory, beyond MIPS-based descriptions, is required to capture the phase transitions of attractive ABPs in inhomogeneous systems. Furthermore, previous studies of two-dimensional systems have reported flocking for attractive ABPs[61], though finite-size analysis indicates that this does not persist as $N \to \infty$[62]. Our three-dimensional simulations show no evidence of global flocking, even when activity gradients drive directed condensate migration. Although we focus here on linear activity gradients, the pressure-balance mechanism does not rely on the gradient being strictly linear. For a smooth monotonic activity profile, we expect condensates to localize near positions where the activity-induced pressure imbalance between the inner and outer interfaces is balanced by cohesive and ideal-pressure contributions. Changing the gradient shape or length scale should therefore shift the balance point and modify the migration rate, while non-monotonic activity profiles may generate multiple localization regions. Looking forward, our results could be experimentally tested by engineering synthetic active condensates based on platforms like enzyme-powered nanomotors[63,64], light-activated Janus particles[47], and robotic swarms[65–67].

## Data availability

The source data for Figs. 1–8 are provided in Supplementary Data 1–8, respectively. Each Supplementary Data file is an Excel workbook containing the numerical data used to generate the corresponding figure panels.

Received: 20 November 2025; Accepted: 16 September 2026;
Published online: 14 October 2026

## References

1. Karsenti, E. Self-organization in cell biology: a brief history. *Nat. Rev. Mol. Cell Biol.* **9**, 255–262 https://doi.org/10.1038/nrm2357 (2008).
2. Hyman, A. A., Weber, C. A. & Jülicher, F. Liquid-liquid phase separation in biology. *Annu. Rev. Cell Dev. Biol.* **30**, 39–58 https://doi.org/10.1146/annurev-cellbio-100913-013325 (2014).
3. Lin, B., Yin, T., Wu, Y. I., Inoue, T. & Levchenko, A. Interplay between chemotaxis and contact inhibition of locomotion determines exploratory cell migration. *Nat. Commun.* **6**, 6619 https://doi.org/10.1038/ncomms7619 (2015).
4. Scarpa, E. & Mayor, R. Collective cell migration in development. *J. Cell Biol.* **212**, 143–155 https://doi.org/10.1083/jcb.201508047 (2016).
5. Wedlich-Söldner, R. & Betz, T. Self-organization: the fundament of cell biology. *Philos. Trans. R. Soc. B* **373**, 20170103 https://doi.org/10.1098/rstb.2017.0103 (2018).
6. Weber, C. A., Zwicker, D., Jülicher, F. & Lee, C. F. Physics of active emulsions. *Rep. Prog. Phys.* **82**, 064601 https://doi.org/10.1088/1361-6633/ab052b (2019).
7. Snead, W. T. & Gladfelter, A. S. The control centers of biomolecular phase separation: how membrane surfaces, ptms, and active processes regulate condensation. *Mol. Cell.* **76**, 295–305 https://doi.org/10.1016/j.molcel.2019.09.016 (2019).
8. Lafontaine, D. L., Riback, J. A., Bascetin, R. & Brangwynne, C. P. The nucleolus as a multiphase liquid condensate. *Nat. Rev. Mol. Cell Biol.* **22**, 165–182 https://doi.org/10.1038/s41580-020-0272-6 (2021).
9. Ziepke, A., Maryshev, I., Aranson, I. S. & Frey, E. Multi-scale organization in communicating active matter. *Nat. Commun.* **13**, 6727 https://doi.org/10.1038/s41467-022-34484-2 (2022).
10. Coupe, S. & Fakhri, N. Nonequilibrium phases of a biomolecular condensate facilitated by enzyme activity. *Soft Matter* **22**, 2656–2665 https://doi.org/10.1039/D5SM01106J (2026).
11. Brangwynne, C. P., Mitchison, T. J. & Hyman, A. A. Active liquid-like behavior of nucleoli determines their size and shape in xenopus laevis oocytes. *Proc. Natl. Acad. Sci.* **108**, 4334–4339 https://doi.org/10.1073/pnas.1017150108 (2011).
12. Feric, M. et al. Coexisting liquid phases underlie nucleolar subcompartments. *Cell* **165**, 1686–1697 https://doi.org/10.1016/j.cell.2016.04.047 (2016).
13. Saha, S. et al. Polar positioning of phase-separated liquid compartments in cells regulated by an mrna competition mechanism. *Cell* **166**, 1572–1584 https://doi.org/10.1016/j.cell.2016.08.006 (2016).
14. Jain, S. et al. Atpase-modulated stress granules contain a diverse proteome and substructure. *Cell* **164**, 487–498 https://doi.org/10.1016/j.cell.2015.12.038 (2016).
15. Banani, S. F., Lee, H. O., Hyman, A. A. & Rosen, M. K. Biomolecular condensates: organizers of cellular biochemistry. *Nat. Rev. Mol. Cell Biol.* **18**, 285–298 https://doi.org/10.1038/nrm.2017.7 (2017).
16. Guilhas, B. et al. ATP-driven separation of liquid phase condensates in bacteria. *Mol. Cell.* **79**, 293–303 https://doi.org/10.1016/j.molcel.2020.06.034 (2020).
17. Linsenmeier, M. et al. Dynamic arrest and aging of biomolecular condensates are modulated by low-complexity domains, RNA and biochemical activity. *Nat. Commun.* **13**, 3030 https://doi.org/10.1038/s41467-022-30521-2 (2022).
18. Jambon-Puillet, E. et al. Phase-separated droplets swim to their dissolution. *Nat. Commun.* **15**, 3919 https://doi.org/10.1038/s41467-024-47889-y (2024).
19. Ewald, A. J., Brenot, A., Duong, M., Chan, B. S. & Werb, Z. Collective epithelial migration and cell rearrangements drive mammary branching morphogenesis. *Dev. Cell.* **14**, 570–581 https://doi.org/10.1016/j.devcel.2008.03.003 (2008).
20. Carmona-Fontaine, C. et al. Contact inhibition of locomotion in vivo controls neural crest directional migration. *Nature* **456**, 957–961 https://doi.org/10.1038/nature07441 (2008).
21. Mayor, R. & Carmona-Fontaine, C. Keeping in touch with contact inhibition of locomotion. *Trends Cell Biol.* **20**, 319–328 https://doi.org/10.1016/j.tcb.2010.03.005 (2010).
22. Theveneau, E. et al. Collective chemotaxis requires contact-dependent cell polarity. *Dev. Cell* **19**, 39–53 https://doi.org/10.1016/j.devcel.2010.06.012 (2010).
23. Riahi, R., Yang, Y., Zhang, D. D. & Wong, P. K. Advances in wound-healing assays for probing collective cell migration. *J. Lab. Autom.* **17**, 59–65 https://doi.org/10.1177/2211068211426550 (2012).
24. Li, L., He, Y., Zhao, M. & Jiang, J. Collective cell migration: Implications for wound healing and cancer invasion. *Burns Trauma* **1**, 2321–3868 https://doi.org/10.4103/2321-3868.113331 (2013).
25. Li, Y. et al. In vivo quantitative imaging provides insights into trunk neural crest migration. *Cell Rep.* **26**, 1489–1500 https://doi.org/10.1016/j.celrep.2019.01.039 (2019).
26. Miskolci, V., Klemm, L. C. & Huttenlocher, A. Cell migration guided by cell–cell contacts in innate immunity. *Trends Cell Biol.* **31**, 86–94 https://doi.org/10.1016/j.tcb.2020.11.002 (2021).
27. Patel, A. et al. ATP as a biological hydrotrope. *Science* **356**, 753–756 https://doi.org/10.1126/science.aaf6846 (2017).
28. Giampieri, S. et al. Localized and reversible tgf$\beta$ signalling switches breast cancer cells from cohesive to single cell motility. *Nat. Cell Biol.* **11**, 1287–1296 https://doi.org/10.1038/ncb1973 (2009).
29. Ellison, D. et al. Cell–cell communication enhances the capacity of cell ensembles to sense shallow gradients during morphogenesis. *Proc. Natl. Acad. Sci.* **113**, E679–E688 https://doi.org/10.1073/pnas.1516503113 (2016).
30. Auschra, S., Holubec, V., Söker, N. A., Cichos, F. & Kroy, K. Polarization-density patterns of active particles in motility gradients. *Phys. Rev. E* **103**, 062601 https://doi.org/10.1103/PhysRevE.103.062601 (2021).
31. Söker, N. A., Auschra, S., Holubec, V., Kroy, K. & Cichos, F. How activity landscapes polarize microswimmers without alignment forces. *Phys. Rev. Lett.* **126**, 228001 https://doi.org/10.1103/PhysRevLett.126.228001 (2021).
32. Row, H. & Brady, J. F. Reverse osmotic effect in active matter. *Phys. Rev. E* **101**, 062604 https://doi.org/10.1103/PhysRevE.101.062604 (2020).
33. Wang, X., Ramírez-Hinestrosa, S., Dobnikar, J. & Frenkel, D. The lennard-jones potential: when (not) to use it. *Phys. Chem. Chem. Phys.* **22**, 10624–10633 https://doi.org/10.1039/C9CP05445F (2020).
34. Thompson, A. P. et al. LAMMPS - a flexible simulation tool for particle-based materials modeling at the atomic, meso, and continuum scales. *Comp. Phys. Comm.* **271**, 108171 https://doi.org/10.1016/j.cpc.2021.108171 (2022).
35. Stukowski, A. Visualization and analysis of atomistic simulation data with ovito–the open visualization tool. *Model. Simul. Mater. Sci. Eng.* **18**, 015012 https://doi.org/10.1088/0965-0393/18/1/015012 (2009).
36. Prymidis, V., Paliwal, S., Dijkstra, M. & Filion, L. Vapour-liquid coexistence of an active Lennard-Jones fluid. *J. Chem. Phys*. **145** https://doi.org/10.1063/1.4963191 (2016).
37. Paliwal, S., Prymidis, V., Filion, L. & Dijkstra, M. Non-equilibrium surface tension of the vapour-liquid interface of active Lennard-Jones particles. *J. Chem. Phys*. **147** https://doi.org/10.1063/1.4989764 (2017).
38. Omar, A. K., Wang, Z.-G. & Brady, J. F. Microscopic origins of the swim pressure and the anomalous surface tension of active matter. *Phys. Rev. E* **101**, 012604 https://doi.org/10.1103/PhysRevE.101.012604 (2020).
39. Omori, T. & Yamaguchi, Y. Molecular anatomy of the pressure anisotropy in the interface of one and two component fluids: Local

thermodynamic description of the interfacial tension. *J. Chem. Phys*. **161**, https://doi.org/10.1063/5.0235858 (2024).
40. Schwarz-Linek, J. et al. Polymer-induced phase separation in Escherichia coli suspensions. *Soft Matter* **6**, 4540–4549 https://doi.org/10.1039/C0SM00214C (2010).
41. Schwarz-Linek, J. et al. Phase separation and rotor self-assembly in active particle suspensions. *Proc. Natl. Acad. Sci.* **109**, 4052–4057 https://doi.org/10.1073/pnas.1116334109 (2012).
42. Ikeshoji, T., Hafskjold, B. & Furuholt, H. Molecular-level calculation scheme for pressure in inhomogeneous systems of flat and spherical layers. *Mol. Simul.* **29**, 101–109 https://doi.org/10.1080/102866202100002518a (2003).
43. Li, L., Sun, Z. & Yang, M. Surface tension between coexisting phases of active brownian particles. *Proc. Natl. Acad. Sci.* **122**, e2505010122 https://doi.org/10.1073/pnas.2505010122 (2025).
44. Ginot, F., Theurkauff, I., Detcheverry, F., Ybert, C. & Cottin-Bizonne, C. Aggregation-fragmentation and individual dynamics of active clusters. *Nat. Commun.* **9**, 696 https://doi.org/10.1038/s41467-017-02625-7 (2018).
45. Mognetti, B. M. et al. Living clusters and crystals from low-density suspensions of active colloids. *Phys. Rev. Lett.* **111**, 245702 https://doi.org/10.1103/PhysRevLett.111.245702 (2013).
46. Caprini, L., Breoni, D., Ldov, A., Scholz, C. & Löwen, H. Dynamical clustering and wetting phenomena in inertial active matter. *Commun. Phys.* **7**, 343 https://doi.org/10.1038/s42005-024-01835-y (2024).
47. Palacci, J., Sacanna, S., Steinberg, A. P., Pine, D. J. & Chaikin, P. M. Living crystals of light-activated colloidal surfers. *Science* **339**, 936–940 https://doi.org/10.1126/science.1230020 (2013).
48. Bechinger, C. et al. Active particles in complex and crowded environments. *Rev. Mod. Phys.* **88**, 045006 https://doi.org/10.1103/RevModPhys.88.045006 (2016).
49. Alert, R. & Trepat, X. Physical models of collective cell migration. *Annu. Rev. Condens. Matter Phys.* **11**, 77–101 https://doi.org/10.1146/annurev-conmatphys-031218-013516 (2020).
50. Vuijk, H. D., Klempahn, S., Merlitz, H., Sommer, J.-U. & Sharma, A. Active colloidal molecules in activity gradients. *Phys. Rev. E* **106**, 014617 https://doi.org/10.1103/PhysRevE.106.014617 (2022).
51. Takatori, S. C. & Brady, J. F. A theory for the phase behavior of mixtures of active particles. *Soft Matter* **11**, 7920–7931 https://doi.org/10.1039/C5SM01792K (2015).
52. Ginot, F. et al. Nonequilibrium equation of state in suspensions of active colloids. *Phys. Rev. X* **5**, 011004 https://doi.org/10.1103/PhysRevX.5.011004 (2015).
53. Speck, T. Stochastic thermodynamics for active matter. *Europhys. Lett.* **114**, 30006 https://doi.org/10.1209/0295-5075/114/30006 (2016).
54. Dai, Q., Chong, Z., Huang, W. & Wang, X. Migration of liquid bridges at the interface of spheres and plates with an imposed thermal gradient. *Langmuir* **36**, 6268–6276 https://doi.org/10.1021/acs.langmuir.9b03951 (2020).
55. Cunha, V. H., Dorao, C. A. & Fernandino, M. Influence of liquid–vapor phase change on the self-propelled motion of droplets on wettability gradient surfaces. *Phys. Fluids* **36** https://doi.org/10.1063/5.0239562 (2024).
56. Omar, A. K., Row, H., Mallory, S. A. & Brady, J. F. Mechanical theory of nonequilibrium coexistence and motility-induced phase separation. *Proc. Natl. Acad. Sci.* **120**, e2219900120 https://doi.org/10.1073/pnas.2219900120 (2023).
57. Tschopp, S. M., Vahid, H., Sharma, A. & Brader, J. M. Combining integral equation closures with force density functional theory for the study of inhomogeneous fluids. *Soft Matter* **21**, 2633–2645 https://doi.org/10.1039/D4SM01262C (2025).
58. Tschopp, S. M., Vahid, H. & Brader, J. M. Routes to the density profile and structural inconsistency. *J. Phys. Chem. B* **130**, 1424–1436 https://doi.org/10.1021/acs.jpcb.5c07785 (2026).
59. Malet-Engra, G. et al. Collective cell motility promotes chemotactic prowess and resistance to chemorepulsion. *Curr. Biol.* **25**, 242–250 https://doi.org/10.1016/j.cub.2014.11.030 (2015).
60. Bussmann, J. & Raz, E. Chemokine-guided cell migration and motility in zebrafish development. *EMBO J.* **34**, 1309–1318 https://doi.org/10.15252/embj.201490105 (2015).
61. Caprini, L. & Löwen, H. Flocking without alignment interactions in attractive active brownian particles. *Phys. Rev. Lett.* **130**, 148202 https://doi.org/10.1103/PhysRevLett.130.148202 (2023).
62. Mahault, B. Comment on flocking without alignment interactions in attractive active brownian particles [arxiv: 2303.07746]. *arXiv preprint arXiv:2309.00015* https://doi.org/10.48550/arXiv.2309.00015 (2023).
63. Song, S. et al. Engineering transient dynamics of artificial cells by stochastic distribution of enzymes. *Nat. Commun.* **12**, 6897 https://doi.org/10.1038/s41467-021-27229-0 (2021).
64. Mason, A. F., Buddingh', B. C., Williams, D. S. & Van Hest, J. C. Hierarchical self-assembly of a copolymer-stabilized coacervate protocell. *J. Am. Chem. Soc.* **139**, 17309–17312 https://doi.org/10.1021/jacs.7b10846 (2017).
65. Santos, V. G. et al. Spatial segregative behaviors in robotic swarms using differential potentials. *Swarm Intell.* **14**, 259–284 https://doi.org/10.1007/s11721-020-00184-0 (2020).
66. Ceron, S., Gardi, G., Petersen, K. & Sitti, M. Programmable self-organization of heterogeneous microrobot collectives. *Proc. Natl. Acad. Sci.* **120**, e2221913120 https://doi.org/10.1073/pnas.2221913120 (2023).
67. Pan, M. et al. Applying the intrinsic principle of cell collectives to program robot swarms. *Cell Rep. Phys. Sci.* **5** https://doi.org/10.1016/j.xcrp.2024.102122 (2024).

## Acknowledgements

We gratefully acknowledge the NHR Center at TU Dresden for providing high-performance computing resources. J.U.S. thanks the cluster of excellence "Physics of Life-" at TU Dresden for its support.

## Author contributions

**Hossein Vahid:** Conceptualization; Data curation; Formal analysis; Investigation; Methodology; Validation; Visualization; Writing—original draft. **Jens-Uwe Sommer:** Conceptualization; Investigation; Methodology; Resources; Supervision; Validation; Writing—review & editing. **Abhinav Sharma:** Conceptualization; Investigation; Methodology; Resources; Supervision; Validation; Writing—review & editing.

## Funding

This work was supported by Deutsche Forschungsgemeinschaft (DFG) under Project No. 561963765 (H.V.) and No. 525864799 (A.S.). Open Access funding enabled and organized by Projekt DEAL.

## Competing interests

The authors declare no competing interests.

## Additional information

**Supplementary information** The online version contains supplementary material available at https://doi.org/10.1038/s42005-026-02903-1.

**Correspondence** and requests for materials should be addressed to Jens-Uwe Sommer or Abhinav Sharma.

**Peer review information** Communications Physics thanks all reviewers for their contribution to the peer review of this work. A peer review file is available.

**Reprints and permissions information** is available at http://www.nature.com/reprints

**Publisher's note** Springer Nature remains neutral with regard to jurisdictional claims in published maps and institutional affiliations.

**Open Access** This article is licensed under a Creative Commons Attribution 4.0 International License, which permits use, sharing, adaptation, distribution and reproduction in any medium or format, as long as you give appropriate credit to the original author(s) and the source, provide a link to the Creative Commons licence, and indicate if changes were made. The images or other third party material in this article are included in the article's Creative Commons licence, unless indicated otherwise in a credit line to the material. If material is not included in the article's Creative Commons licence and your intended use is not permitted by statutory regulation or exceeds the permitted use, you will need to obtain permission directly from the copyright holder. To view a copy of this licence, visit http://creativecommons.org/licenses/by/4.0/.

© The Author(s) 2026